Microstructure and mechanical properties of hyperuniform heterogeneous materials

Yaopengxiao Xu, Shaohua Chen, Pei-En Chen, Wenxiang Xu, and Yang Jiao

Phys. Rev. E **96**, 043301 — Published 2 October 2017

DOI: 10.1103/PhysRevE.96.043301

Microstructure and mechanical properties of hyperuniform heterogeneous materials

Yaopengxiao Xu[1], Shaohua Chen[1], Pei-En Chen[2], Wenxiang Xu[3,*], and Yang Jiao[1*]
[1]*Materials Science and Engineering, Arizona State University, Tempe, AZ 85287;* [2]*Mechanical Engineering, Arizona State University, Tempe, AZ 85287;* [3]*Institute of Soft Matter Mechanics, College of Mechanics and Materials, Hohai University, Nanjing 211100, P.R. China*

A hyperuniform random heterogeneous material is one in which the local volume fraction fluctuations in an observation window decay faster than the reciprocal window volume as the window size increases. Recent studies show that this new class of materials are endowed with superior physical properties such as large isotropic photonic band gaps and optimal transport properties. Here, we employ a stochastic optimization procedure to systematically generate realizations of hyperuniform heterogeneous materials with controllable short-range order, which is partially quantified using the two-point correlation function $S_2(r)$ associated with the phase of interest. Specifically, our procedure generalizes the widely-used Yeong-Torquato reconstruction procedure by including an additional constraint for hyperuniformity, i.e., the volume integral of the auto-covariance function $\chi(r) = S_2(r) - \phi^2$ over the whole space is zero. In addition, we only require the reconstructed S_2 to match the target function up to a certain cut-off distance γ, in order to give the system sufficient degrees of freedom to satisfy the hyperuniform condition. By systematically increasing the γ value for a given S_2, one can produce a spectrum of hyperuniform heterogeneous materials with varying degrees of partial short-range order compatible with the specified S_2. The mechanical performance including both elastic and brittle fracture behaviors of the generated hyperuniform materials is analyzed using a volume-compensated lattice-particle method. For purpose of comparison, the corresponding non-hyperuniform materials with the same short-range order (i.e., with S_2 constrained up to the same γ value) are also constructed and their mechanical performance is analyzed. Here, we consider two specific S_2 including the positive exponential decay function and the correlation function associated with an equilibrium hard sphere system. For the constructed systems associated with these two specific functions, we find although the hyperuniform materials are softer than their non-hyperuniform counterparts, the former generally possesses a significantly higher brittle fracture strength than the latter. This superior mechanical behavior is attributed to the lower degree of stress concentration in the material resulting from the hyperuniform microstructure, which is crucial to crack initiation and propagation.

PACS numbers: 05.20.-y, 61.43.-j

I. INTRODUCTION

The concept of hyperuniformity was first introduced by Torquato and Stillinger for many-particle systems [1] and was subsequently generalized by Zachary and Torquato to heterogeneous materials [2]. Specifically, a hyperuniform point pattern (e.g., a collection of particle centers in a many-body system) is one in which the local number density fluctuations grow slower than the volume of an observation window as the window size increases, implying that the infinite-wavelength number density fluctuations completely vanish. Similarly, a hyperuniform random heterogeneous material is one in which the local volume fraction fluctuations in an observation window decay faster than the reciprocal window volume as the window size increases and the infinite-wavelength local volume fraction fluctuations are completely suppressed.

The property of hyperuniformity has been identified in many physical and biological systems, including the density fluctuations in early universe [3], maximally random jammed packing of hard particles [4–7], certain exotic classical ground states of many-particle systems [8–15], jammed colloidal systems [16–19], driven nonequilibrium systems [20–23], certain quantum ground states [24, 25], avian photoreceptor patterns [26], organization of adapted immune systems [27], and amorphous silicon [28, 29], to name but a few. It has been suggested that hyperuniformity can be considered as a new state of matter [1], which possesses a hidden order in between of that of a perfect crystal and a totally disordered system (e.g., a Poisson distribution of points). In addition, it has been shown that hyperuniform heterogeneous materials can be designed to possess superior physical properties including large isotropic photonic band gaps [30–32] and optimized transport properties [33]. Very recently, the notation of hyperuniformity has been further generalized to vector fields, anisotropic and inhomogeneous systems [34, 35]. In addition, materials with hyperuniform structures have also been successfully fabricated or synthesized using different techniques [36, 37].

A hyperuniform many-particle system with a specific degree of spatial order can be reconstructed using the collective coordinate approach (CCA) [10–12, 14, 15].

*Electronic address: xuwenxiang@hhu.edu.cn(W.X.);yang.jiao.2@asu.edu(Y.J.)

Specifically, in CCA an initial random configuration of particles is evolved using stochastic optimization to a final state possessing a prescribed structure factor $S(k)$ with the small-wavenumber limit $\lim_{k\to 0} S(k) = 0$ to ensure hyperuniformity. The degree of order in the system can be controlled by imposing different forms of $S(k)$, satisfying the condition $\lim_{k\to 0} S(k) = 0$. This approach has recently been generalized to reconstruct hyperuniform heterogeneous materials possessing a prescribed spectral density $\hat{\chi}(k)$ with $\lim_{k\to 0} \hat{\chi}(k) = 0$ [34]. In this case, an initial random distribution of pixels representing the phase of interest is evolved using stochastic optimization to a final microstructure with the prescribed $\hat{\chi}(k)$. The hyperuniform condition $\lim_{k\to 0} \hat{\chi}(k) = 0$ for heterogeneous materials is discussed in detail in Sec. II.

In this paper, we devise an alternative procedure to systematically generate realizations of hyperuniform heterogeneous materials with controllable short-range order. Instead of evolving the material microstructure to achieve a prescribed spectral density $\hat{\chi}(k)$, in our reconstruction the final microstructure is required to partially match a set of prescribed spatial correlation functions (e.g., the two-point correlation function S_2) for the phase of interest while simultaneously satisfying the hyperuniform condition $\lim_{k\to 0} \hat{\chi}(k) = 0$. This is achieved by generalizing the Yeong-Torquato reconstruction procedure [38] to include an additional energy term for the hyperuniform condition, which can be also expressed as the volume integral of the auto-covariance function $\chi(r) = S_2(r) - \phi^2$ over the whole space being zero. Different from previous reconstruction/construction studies, we only require the reconstructed S_2 to match the target function up to a certain cut-off distance γ, in order to give the system sufficient degrees of freedom to satisfy the hyperuniform condition. By systematically increasing the γ value, one can produce a spectrum of hyperuniform heterogeneous materials with varying degrees of partial short-range order compatible of the specified correlation function. In this work, we consider two specific S_2 including the positive exponential decay function and the correlation function associated with an equilibrium hard sphere system.

For purpose of comparison, the corresponding non-hyperuniform materials, defined as materials possess the same correlation function as the hyperuniform counterpart for $r \leq \gamma$ but do not satisfy the hyperuniform condition, are also generated. A hyperuniform material and its non-hyperuniform counterpart possess microstructures that are statistically indistinguishable from one another on small length scales.

We also study the mechanical performance of the generated hyperuniform and corresponding non-hyperuniform materials, including both elastic and failure behaviors using a volume-compensated lattice-particle method. For the specific materials associated with the two correlation functions studied here, we find although the hyperuniform materials are softer than their non-hyperuniform counterparts, i.e., with a smaller Young's modulus, the hyperuniform materials generally possess a superior brittle fracture behavior, including both a higher resistance to crack initiation and a larger fracture strength. We find this superior mechanical behavior is attributed to the lower degree of stress concentration in the material resulting from the hyperuniform microstructure, which is crucial to crack initiation and propagation.

The rest of the paper is organized as follows: In Sec. II, we provide definitions of quantities that are relevant to hyperuniform heterogeneous materials. In Sec. III, we present the stochastic reconstruction procedure for generating hyperuniform heterogeneous materials with varying degrees of short-range order. In Secs. IV and V, we respectively provide detailed analysis on the structural and mechanical properties of the generated hyperuniform materials and their non-hyperuniform counterparts. In Sec. VI, we make concluding remarks.

II. DEFINITIONS FOR HYPERUNIFORM HETEROGENEOUS MATERIALS

A. n-Point Correlation Function

In general, the microstructure of a heterogeneous material can be uniquely determined by specifying the indicator functions associated with all of the individual phases of the material [39, 40]. Without loss of generality, we focus on two-phase materials (binary medium) in this work. We note that the generalization of the subsequent discussion to a multiple phase system is straightforward.

Consider a statistically homogeneous material M occupying the region $\mathcal{V}$ in the d-dimensional Euclidean space $\mathbb{R}^d$ ($d = 1, 2, 3$) which is partitioned into two disjoint phases: phase 1, a region $\mathcal{V}_1$ of volume fraction ϕ_1 and phase 2, a region $\mathcal{V}_2$ of volume fraction ϕ_2. It is obvious that $\mathcal{V}_1 \cup \mathcal{V}_2 = \mathcal{V}$ and $\mathcal{V}_1 \cap \mathcal{V}_2 = \mathbf{0}$. The indicator function $\mathcal{I}^{(i)}(\mathbf{x})$ of phase i is given by

$$\mathcal{I}^{(i)}(\mathbf{x}) = \begin{cases} 1 & \mathbf{x} \in \mathcal{V}_i, \\ 0 & \mathbf{x} \in \bar{\mathcal{V}}_i, \end{cases} \tag{1}$$

for $i = 1, 2$ with $\mathcal{V}_i \cup \bar{\mathcal{V}}_i = \mathcal{V}$ and

$$\mathcal{I}^{(1)}(\mathbf{x}) + \mathcal{I}^{(2)}(\mathbf{x}) = 1. \tag{2}$$

The n-point correlation function $S_n^{(i)}$ for phase i is defined as follows:

$$S_n^{(i)}(\mathbf{x}_1, \mathbf{x}_2, ..., \mathbf{x}_n,) = \left\langle \mathcal{I}^{(i)}(\mathbf{x}_1)\mathcal{I}^{(i)}(\mathbf{x}_2)...\mathcal{I}^{(i)}(\mathbf{x}_n) \right\rangle, \tag{3}$$

where the angular brackets "$\langle ... \rangle$" denote ensemble averaging over independent realizations of the medium.

The two-point correlation function $S_2^{(i)}$ for phase i, the focus of this study, is defined by

$$S_2^{(i)}(\mathbf{x}_1, \mathbf{x}_2) = \left\langle \mathcal{I}^{(i)}(\mathbf{x}_1)\mathcal{I}^{(i)}(\mathbf{x}_2) \right\rangle. \tag{4}$$

As pointed out in Sec. I, for a statistically homogeneous medium, $S_2^{(i)}$ is a function of the relative displacements of point pairs, i.e.,

$$S_2^{(i)}(\mathbf{x}_1, \mathbf{x}_2) = S_2^{(i)}(\mathbf{x}_2 - \mathbf{x}_1) = S_2^{(i)}(\mathbf{r}), \tag{5}$$

where $\mathbf{r} = \mathbf{x}_2 - \mathbf{x}_1$. In the infinite volume limit, if the medium is also ergodic the ensemble average is equivalent to the volume average, i.e.,

$$S_2^{(i)}(\mathbf{r}) = \lim_{V\to\infty} \frac{1}{V} \int_V \mathcal{I}^{(i)}(\mathbf{x})\, \mathcal{I}^{(i)}(\mathbf{x}+\mathbf{r})\, d\mathbf{x} \tag{6}$$

If the medium is also statistically isotropic, $S_2^{(i)}$ is a radial function, depending on the separation distances of point pairs only, i.e.,

$$S_2^{(i)}(\mathbf{x}_1, \mathbf{x}_2) = S_2^{(i)}(|\mathbf{r}|) = S_2^{(i)}(r). \tag{7}$$

Interested readers are referred to Ref. [40] for a detailed discussion of $S_2^{(i)}$ and other higher order $S_n^{(i)}$. Henceforth, we will drop the superscript i in $S_2^{(i)}$ for simplicity. Without further elaboration, S_2 is always the two-point correlation function of the phase of interest.

The two-point correlation function S_2 can be efficiently computed from given digital images of a material, in which the microstructure is represented as a 2D (or 3D) array of pixels (or voxels), in which value of each pixel indicates the local state (e.g., phases) of that pixel. For a binary system, the array is simply a collection of black and white pixels on a regular lattice. The probabilistic interpretation of the correlation functions enable us to develop a general sampling method for the reconstruction of statistically homogeneous and isotropic digitized textures based on the "lattice-gas" formalism, which is introduced in Refs. [41, 42] and generalized in Ref. [43]. In the generalized formalism, pixels with different values (occupying the lattice sites) correspond to distinct local states and pixels with the same value are considered to be "molecules" of the same "gas" species. In the case of S_2, all "molecules" are of the same species. We denote the number of lattice-site separation distances of length r by $N_S(r)$ and the number of molecule-pair separation distances of length r by $N_P(r)$. Thus, the fraction of pair distances with both ends occupied by the phase of interest, i.e., the two-point correlation function, is given by $S_2(r) = N_P(r)/N_S(r)$.

B. Hyperuniformity in heterogeneous materials

A hyperuniform heterogeneous material has the property that the variance in the volume fraction of the phase of interest in an observation window Ω decays more quickly than the reciprocal volume of that window [2]. In the case of a spherical observation window, this definition implies that the variance $\sigma_\tau^2(R)$ in the local volume fraction $\tau(\mathbf{x})$ decays more quickly than R^{-d} in d dimensions, where R is the radius of the observation window.

In particular, the local volume fraction $\tau(\mathbf{x})$ of the phase of interest is defined as:

$$\tau_i(\mathbf{x}; \mathbf{R}) = \frac{1}{v(R)} \int \mathcal{I}(\mathbf{z}) w(\mathbf{z} - \mathbf{x}; R) d\mathbf{z}, \tag{8}$$

where $v(R)$ is the volume of the observation window, w is the corresponding indicator function, and $\mathcal{I}$ is the indicator function of the phase of interest. Using this definition, the variance σ_τ^2 in the local volume fraction is given by:

$$\sigma_\tau^2 = \frac{1}{v(R)} \int_{\mathbb{R}^d} \chi(\mathbf{r}) \alpha(\mathbf{r}; R) d\mathbf{r}, \tag{9}$$

where $\chi(\mathbf{r})$ is the autocovariance function, i.e., $\chi(\mathbf{r}) = S_2(\mathbf{r}) - \phi^2$, and $\alpha(\mathbf{r}; R)$ is the scaled intersection volume which has the support $[0, 2R]$, the range $[0, 1]$, and the following integral representation:

$$\alpha(r; R) = c(d) \int_0^{\cos^{-1}[r/(2R)]} \sin^d(\theta) d\theta, \tag{10}$$

where $c(d)$ is a d-dimensional constant given by

$$c(d) = \frac{2\Gamma(1 + d/2)}{\pi^{1/2}\Gamma[(d+1)/2]}. \tag{11}$$

The variance in the local volume fraction admits the asymptotic expansion [2]:

$$\sigma_\tau^2 = \frac{\rho}{2^d \phi} \left\{ A_\tau \left(\frac{D}{R}\right)^d + B_\tau \left(\frac{D}{R}\right)^{d+1} + o\left[\left(\frac{D}{R}\right)^{d+1}\right] \right\} \tag{12}$$

$$A_\tau = \int_{\mathbb{R}^d} \chi(\mathbf{r}) d\mathbf{r} = \lim_{\|\mathbf{k}\|\to 0} \hat{\chi}(\mathbf{k}) \tag{13}$$

$$B_\tau = -\frac{\kappa(d)}{D} \int_{\mathbb{R}^d} \|\mathbf{r}\| \chi(\mathbf{r}) d\mathbf{r} = \frac{1}{\pi v(1) D} \int_{\mathbb{R}^d} \frac{\hat{\chi}(\mathbf{k})}{\|\mathbf{k}\|^{d+1}} d\mathbf{k}. \tag{14}$$

The coefficients A_τ and B_τ in (13) and (14) control the asymptotic scaling of the fluctuations in the local volume fraction. By definition, a hyperuniform heterogeneous material possesses a local volume fraction variance $\sigma_\tau^2 \sim R^{-(d+1)}$ as $R \to +\infty$, which requires the coefficient A_τ of the leading term in the asymptotic expansion (12) vanishes, i.e.,

$$A_\tau = \lim_{\|\mathbf{k}\|\to 0} \hat{\chi}(\mathbf{k}) = 0. \tag{15}$$

In other words, for a hyperuniform material, its spectral density $\hat{\chi}$ goes to zero in the zero wave-vector limit. For statistically homogeneous and isotropic materials, the hyperuniform condition (15) reduces to

$$A_\tau = \lim_{k\to 0} \hat{\chi}(k) = \int_r [S_2(r) - \phi^2] \Omega_d(r) dr = 0, \tag{16}$$

where $\Omega_d(r)$ is the surface area of a sphere with radius r in d dimensions, and the integral is over the entire space the system is defined.

III. GENERATING REALIZATIONS OF HYPERUNIFORM MATERIALS USING STOCHASTIC OPTIMIZATION

Generating realizations of heterogeneous materials from limited morphological information is a topic of great interest [41–60]. Our procedure for reconstructing hyperuniform heterogeneous materials is developed within the Yeong-Torquato (YT) stochastic reconstruction framework [38], in which an initial random microstructure is evolved to minimize an energy function that measures the difference between the target correlation functions and the corresponding functions of the simulated microstructure.

In the YT procedure, the reconstruction problem is formulated as an "energy" minimization problem, with the energy functional E defined as follows

$$E = \sum_r \sum_\alpha \left[f_n^\alpha(r) - \widehat{f}_n^\alpha(r) \right]^2, \tag{17}$$

where $\widehat{f}_n^\alpha(r)$ is a target correlation function of type α and $f_n^\alpha(r)$ is the corresponding function associated with a trial microstructure. The simulated annealing method [61] is usually employed to solve the aforementioned minimization problem. Specifically, starting from an initial trial microstructure (i.e., old microstructure) which contains a fixed number of pixels (voxels) for each phase consistent with the volume fraction of that phase, two randomly selected pixels (voxels) associated with different phases are exchanged to generate a new trial microstructure. Relevant correlation functions are sampled from the new trial microstructure and the associated energy is computed, which determines whether the new trial microstructure should be accepted or not via the probability:

$$p_{acc} = min\{\exp(-\Delta E/T), 1\}, \tag{18}$$

where ΔE is the energy difference between the new and old trial microstructure and T is a virtual temperature that is chosen to be initially high and slowly decreases according to a cooling schedule [38]. An appropriate cooling schedule reduces the chances that the system gets trapped in a shallow local energy minimum. In practice, a power law schedule $T(n) = \alpha^n T_0$ is usually employed, where T_0 is the initial temperature, n is the cooling stage and $\alpha \in (0, 1)$ is the cooling factor. The simulation is terminated when E is smaller than a prescribed tolerance (e.g., 10^{-8}). Generally, a large number of trial microstructures need to be searched to generate a successful reconstruction. Therefore, highly efficient sampling methods [41–43] are used that enable one to rapidly obtain the prescribed correlation functions of a new microstructure by updating the corresponding functions associated with the old microstructure, instead of completely re-computing the functions.

Here, we generalize the YT procedure by introducing an additional constraint for hyperuniformity. In addition, we allow the given two-point correlation function to be constrained only up to a certain cut-off distance γ for controlling the short-range order in the system. This is different from previous reconstruction studies in which the all values of S_2 are constrained. Specifically, the "energy" for the reconstruction now contains two terms, i.e.,

$$E = E_1 + E_2, \tag{19}$$

where E_1 and E_2 are respectively associated with the target correlation function $\widehat{S}_2$ and the hyperuniform constraint, i.e.,

$$E_1 = \sum_{r=0}^{\gamma} \left[S_2(r) - \widehat{S}_2(r) \right]^2, \tag{20}$$

where $\gamma \in [0, L/2)$ (L is the linear system size) and

$$E_2 = |\sum_{r=0}^{L/2} \left[S_2(r) - \phi^2 \right] \Omega_d(r)|^2, \tag{21}$$

where $\Omega_d(r)$ is surface area of a sphere with radius r in d dimensions. For $d = 2$, the main focus of this paper, $\Omega_2(r) = 2\pi r$. We note that Eq.(21) is the discrete form of the hyperuniform condition (16) in which the integral over the entire space is replaced by the summation over all r values consistent with the periodic boundary condition.

We note that the ground state of the reconstruction requires $E_1 = E_2 = 0$. The summation in Eq. (21) is the discrete form of the integral in Eq. (16), and thus, the condition $E_2 = 0$ also implies $A_\tau = 0$. In addition, we employ periodic boundary condition in the reconstructions and the largest distance in S_2 is given by half of the linear system size $L/2$. However, the constraints imposed by $E_1 = 0$ and $E_2 = 0$ are not independent of one another. For example, if an arbitrary given S_2 is completely constrained up to $r = L/2$, there is no guarantee that the hyperuniform condition (16) can be satisfied. Therefore, we will only constrain S_2 up to the cut-off distance γ to impose partial short-range order consistent with the given S_2, and always require $E_2 = 0$ to ensure hyperuniformity is achieved. As we will show below, the unconstrained values for S_2 can be significantly different from those of the target function in order to achieve hyperuniformity.

IV. MICROSTRUCTURE OF HYPERUNIFORM HETEROGENEOUS MATERIALS

A. Correlation functions for controlling partial short-range order

Two types of 2-point correlation functions are employed here to control the partial short-range order of the reconstructed hyperuniform materials, i.e., the exponential decay function S_2^{ED} and the hard sphere function

S_2^{HS}. It is also convenient to introduce the scaled autocovariance function, i.e.,

$$f(r) = \frac{S_2(r) - \phi^2}{\phi(1-\phi)}, \tag{22}$$

where ϕ is the volume fraction of the phase of interest. Different from S_2, the scaled autocovariance function is independent of the reference phase and phase volume fraction, and characterizes the intrinsic spatial correlations in the material system.

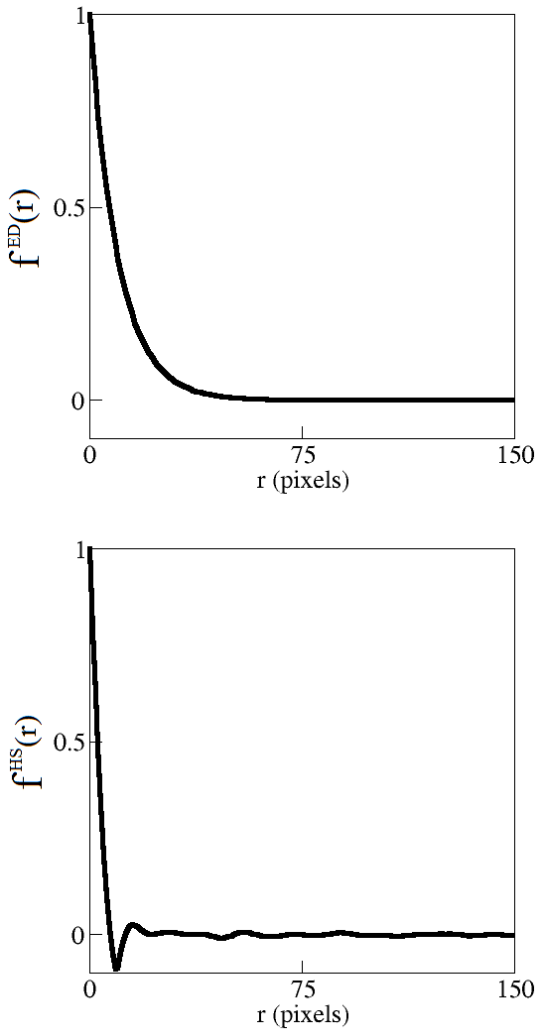

FIG. 1: Correlation functions employed to control the short-range order in the reconstructed hyperuniform materials. Upper panel: The exponential decay function f^{ED}. Lower panel: The hard sphere function f^{HS}.

The exponential decay function is given by

$$f^{ED} = exp(-r/a), \tag{23}$$

where a is a characteristic correlation length of the material and we use $a = 10$ pixels for the subsequent reconstructions. This monotonic decreasing correlation function, as shown in Fig. 1, is also referred to as the Debye random medium function [41], which corresponds to materials containing random clusters of arbitrary sizes and shapes. The hard sphere function f^{HS} does not possess an analytical expression. Therefore, we compute f^{HS} from an ensemble of 2D hard sphere packings sampled from a Monte Carlo simulation of an equilibrium 2D hard sphere fluid [40]. As shown in Fig. 1, f^{HS} contains significant oscillations for small distances, indicating the spatial correlations among the spheres due to the non-overlapping constraint. The diameter of the sphere, which corresponds to the r value associated with first minimum of the oscillating function, is $D = 10$ pixels. For the subsequent reconstructions, we will consider two values of volume fraction, $\phi = 0.3$ and $\phi = 0.5$, which are respectively below and above the percolation threshold for the corresponding materials. The two-point function $S_2(r)$ can be readily obtained from the corresponding $f(r)$ using Eq. (22).

The choice of aforementioned correlation functions is inspired by Refs. [34, 35]. Specifically, since the exponential function $f^{ED}(r)$ is always positive, it is not possible for Eq. (16) to hold for this function (i.e., the integral is always greater than zero for all volume fractions). This implies that the partial short-range order imposed by $f^{ED}(r)$ will be competing with the global hyperuniformity constraint, and hyperuniformity is successively more difficult to achieve as the cut-off distance γ increases. On the other hand, the oscillating hard sphere function $f^{HS}(r)$ is more compatible with the hyperuniform condition (16), suggesting that it is easier to achieve hyperuniformity in system with such $f^{HS}(r)$. As we will show in Sec. IV, the reconstructed hyperunfiorm materials associated with these two different correlation functions can possess distinct properties compared to their non-hyperuniform counterparts.

B. Realizations of hyperuniform materials

The realizations of hyperuniform materials with a linear size of 300 pixels associated with the aforementioned correlation functions $f^{ED}(r)$ and $f^{HS}(r)$ with increasing constraint distance $\gamma = 5, 10, 15, 25, 50, 80, 100$ and 120 pixels as well as their non-hyperuniform counterparts are generated using the generalized stochastic reconstruction procedure described in Sec. III. For all of the reconstructions, we require that the final energy $E < 10^{-8}$. In the case of hyperuniform materials, this implies that the hyperuniform constraint $E_2 < 10^{-8}$ and the degree of hyperuniformity is also independently verified by directly computing the local volume fraction fluctuations as a function of observation window size.

Figures 2 and 3 respectively show the reconstructed microstructures associated with $f^{ED}(r)$ at volume fractions $\phi = 0.3$ and 0.5 for selected γ values (i.e., 15, 25, 50 and 100 pixels). For all γ values, the constraint (21) is satisfied to a high degree for the hyperuniform systems with $E_2 \sim 10^{-8}$, in contrast to the large $E_2 \sim 10^2$

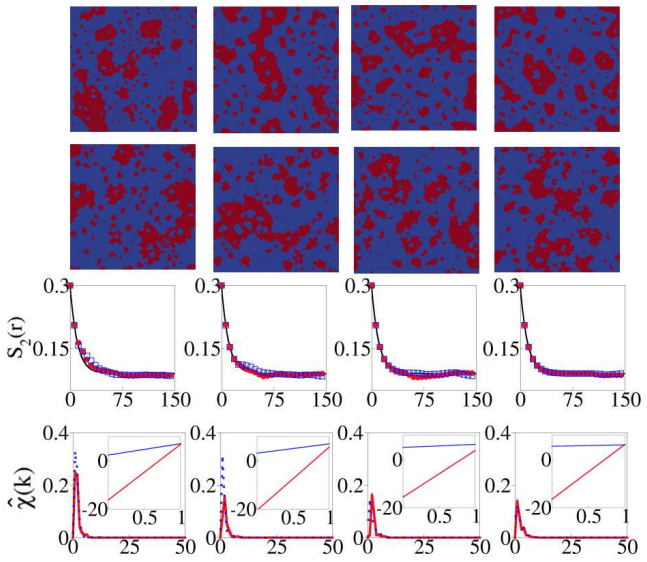

FIG. 2: Realizations of the hyperuniform materials (first row) and the corresponding non-hyperuniform materials (second row) associated with the exponential decay function f^{ED} for different cut-off distances γ with $\phi = 0.3$ for the inclusion phase. The associated target (solid curve) and reconstructed correlation functions (solid circles for hyperuniform materials and empty square for non-hyperuniform materials) are shown in the panels on the third row. The spectral densities $\hat{\chi}(k)$ for the reconstructed materials (solid red curve or light gray in print version for hyperuniform materials, and dashed blue curve or dark gray in print version for non-hyperuniform materials) are shown in the fourth row. The insets (with vertical axis in log scale) show the small k behavior of $\hat{\chi}(k)$. The constraint distances γ from left to right are 15, 25, 50 and 100 pixels.

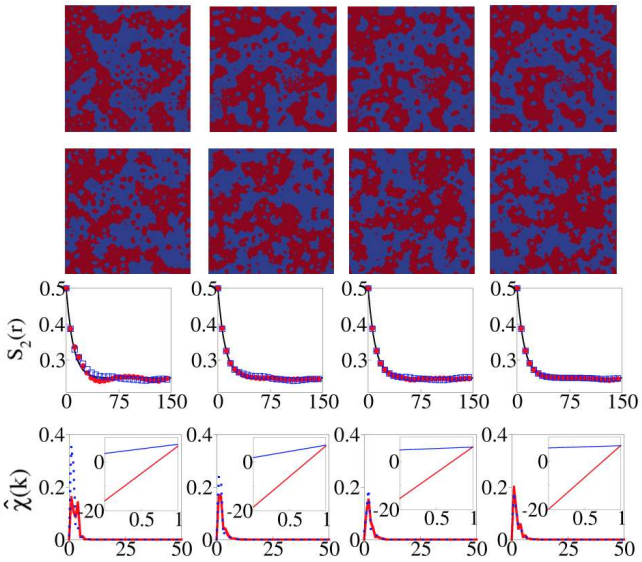

FIG. 3: Realizations of the hyperuniform materials (first row) and the corresponding non-hyperuniform materials (second row) associated with the exponential decay function f^{ED} for different cut-off distances γ with $\phi = 0.5$ for the inclusion phase. The associated target (solid curve) and reconstructed correlation functions (solid circles for hyperuniform materials and empty square for non-hyperuniform materials) are shown in the panels on the third row. The spectral densities $\hat{\chi}(k)$ for the reconstructed materials (solid red curve or light gray in print version for hyperuniform materials, and dashed blue curve or dark gray in print version for non-hyperuniform materials) are shown in the fourth row. The insets (with vertical axis in log scale) show the small k behavior of $\hat{\chi}(k)$. The constraint distances γ from left to right are 15, 25, 50 and 100 pixels.

for the non-hyperuniform systems. This is also consistent with the small k behavior of the spectral densities $\hat{\chi}(k)$ associated with reconstructed systems (see insets in the fourth row of Figs. 2 and 3). It can be seen that for both ϕ values, the reconstructed microstructures contain "clusters of arbitrary sizes and shapes", which is a well-known structural feature of the so called Debye random media [41] associated with the exponential decay S_2. Also shown are the target and reconstructed correlation functions for different cut-off distance γ.

In the case of $\phi = 0.3$, it can be clearly seen that for small γ values (i.e., 15 and 25 pixels), the reconstructed correlation functions for both the hyperuniform and non-hyperuniform cases deviate significantly from the corresponding target functions. For intermediate γ values (e.g., 50 pixels), the reconstructed S_2 for the non-hyperuniform case well matches the target function even for r values beyond the constrained distance. However, for the hyperuniform case, the reconstructed S_2 starts to exhibit a significant decay immediately beyond γ. We note that this behavior is necessary to achieve the hyperuniformity imposed by the constraint (21). Even for large γ values (e.g., 100 pixels), the reconstructed S_2 for the hyperuniform materials still exhibits weak yet non-vanishing oscillations beyond the constrained distance. Again, these oscillations are required by the hyperuniform constraint (21).

The behaviors of the reconstructed systems with $\phi = 0.5$ for both hyperuniform and non-hyperuniform cases as γ increases are very similar to the corresponding systems with $\phi = 0.3$. We note that for both volume fractions, the reconstructed hyperuniform systems and their non-hyperuniform counterparts are almost visually indistinguishable in a statistical sense. This is because by construction these systems possess the same partial short-range spatial correlations (imposed by the same S_2 up to the cut-off distance γ). Yet the two types of systems possess distinctly different structural characteristics on large length scales as indicated by the distinct E_2 values.

Figures 4 and 5 respectively show the reconstructed systems associated with $f^{HS}(r)$ at volume fractions $\phi = 0.3$ and 0.5 for selected γ values (i.e., 15, 25, 50 and 100 pixels). In the reconstructed hyperuniform systems, the constraint (21) is satisfied to a high degree for all γ val-

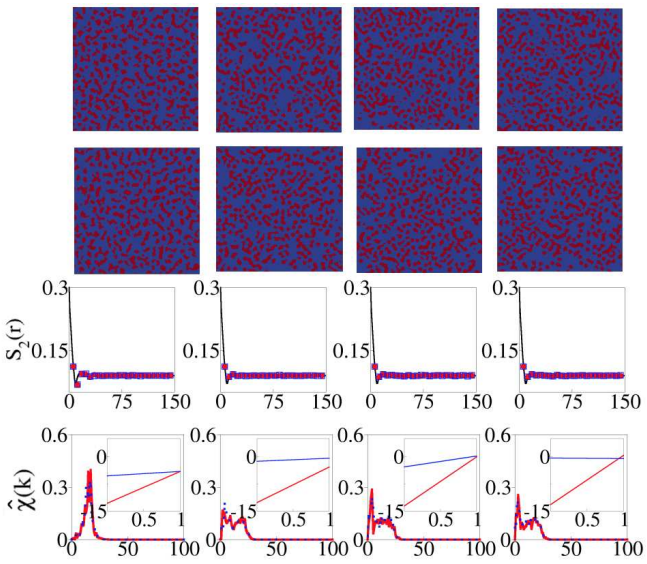

FIG. 4: Realizations of the hyperuniform materials (first row) and the corresponding non-hyperuniform materials (second row) associated with the hard sphere function f^{HS} for different cut-off distances γ with $\phi = 0.3$ for the inclusion phase. The associated target (solid curve) and reconstructed correlation functions (solid circles for hyperuniform materials and empty square for non-hyperuniform materials) are shown in the panels on the third row. The spectral densities $\hat{\chi}(k)$ for the reconstructed materials (solid red curve or light gray in print version for hyperuniform materials, and dashed blue curve or dark gray in print version for non-hyperuniform materials) are shown in the fourth row. The insets (with vertical axis in log scale) show the small k behavior of $\hat{\chi}(k)$. The constraint distances γ from left to right are 15, 25, 50 and 100 pixels.

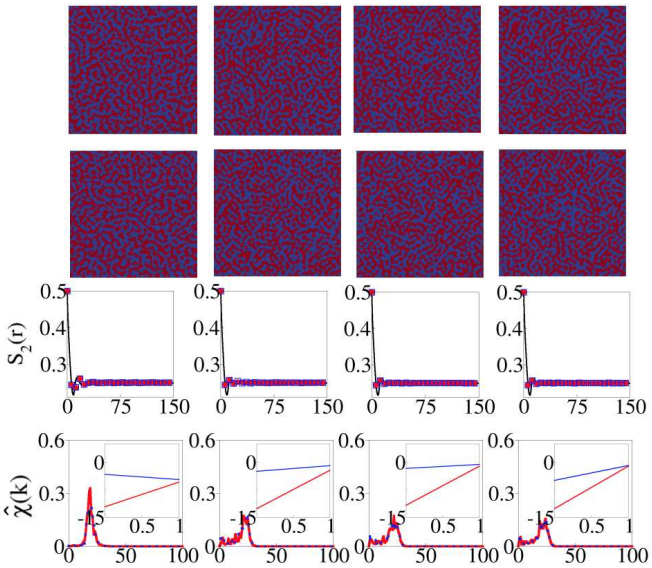

FIG. 5: Realizations of the hyperuniform materials (first row) and the corresponding non-hyperuniform materials (second row) associated with the hard sphere function f^{HS} for different cut-off distances γ with $\phi = 0.5$ for the inclusion phase. The associated target (solid curve) and reconstructed correlation functions (solid circles for hyperuniform materials and empty square for non-hyperuniform materials) are shown in the panels on the third row. The spectral densities $\hat{\chi}(k)$ for the reconstructed materials (solid red curve or light gray in print version for hyperuniform materials, and dashed blue curve or dark gray in print version for non-hyperuniform materials) are shown in the fourth row. The insets (with vertical axis in log scale) show the small k behavior of $\hat{\chi}(k)$. The constraint distances γ from left to right are 15, 25, 50 and 100 pixels.

ues with $E_2 \sim 10^{-8}$. Interestingly, the non-hyperuniform systems associated with the hard-sphere function $f^{HS}(r)$ possess a much smaller $E_2 \sim 10^{-3}$ compared to that for non-hyperuniform systems associated with the exponential function $f^{ED}(r)$, although this value is still much larger than that for the hyperuniform systems. This is also consistent with the small k behavior of the spectral densities $\hat{\chi}(k)$ associated with reconstructed systems (see insets in the fourth row of Figs. 4 and 5). As we discussed in Sec. IV.A, the oscillatory feature of $f^{HS}(r)$ makes it naturally possess a smaller E_2. In addition, the target $f^{HS}(r)$ is associated with the equilibrium hard sphere system, which is already in a state close to hyperuniformity [4].

For $\phi = 0.3$, the reconstructed microstructures contain statistically homogeneous dispersions of compact clusters (i.e. "hard particles") with relatively small aspect ratios. It has been shown that the original spherical particles cannot be perfectly reproduced in the reconstructions using S_2 alone since critical topologically connectedness information of the system is missing. For $\phi = 0.5$, the local spatial correlations are realized by the interconnected stripe-like local structures with well-defined characteristic width λ, resembling those in a typical Eutectic microstructure. A closer inspection reveals that $\lambda \approx D$, where D is the distance associated with the first local minimum in $f^{HS}(r)$, roughly corresponding to the diameter of the spheres in the original system.

Different from the systems associated with $f^{ED}(r)$, neither the reconstructed correlation functions nor the realizations significantly vary as the constraint distance γ increases in the current systems. We note that the oscillations in $f^{HS}(r)$ stems from the strong short-range correlations in the original hard sphere system due to the hard-core repulsions. A direct manifestation of the hard-core repulsion in $f^{HS}(r)$ is the deep first local minimum (valley) and the first local maximum (peak), which respectively corresponds to the size of the hard spheres (i.e., exclusion shell) and the size of the nearest neighbor shell. Once these two crucial length scales are set, the remaining correlations (i.e., oscillations) are also determined. In our reconstructions, all of the cut-off distances used are large than the sphere diameter, i.e., $\gamma > D = 10$ pixels. The reconstructed functions thus have virtually

no freedom to adopt values significantly different from those in the target, even beyond the constrained distance. This leads to the good agreement of the reconstructed and target correlation functions for all distances beyond the cut-off γ.

In addition, the reconstructed hyperuniform systems for both volume fractions are visually indistinguishable from the corresponding non-hyperuniform systems in a statistical sense. This is again because by construction these systems possess the same partial short-range spatial correlations, which are most sensitive to eyeball tests. On the other hand, the large scale structural characteristics are more difficult to be picked up via visual inspection. We note that in this case, the distinction between the hyperuniform and non-hyperuniform systems on large length scales is less dramatic than in the systems associated with the exponential decay function. This also leads to a less dramatic difference in the mechanical properties of the hyperuniform and corresponding non-hyperuniform systems as shown in Sec. V.

V. SUPERIOR MECHANICAL PROPERTIES OF HYPERUNIFORM HETEROGENEOUS MATERIALS

A. Lattice-particle method for micromechanical analysis

The elastic and fracture behaviors of the generated hyperuniform heterogeneous materials are analyzed using the volume-compensated lattice-particle method (LPM) [62, 63]. In the LPM, the continuum is treated as an ordered network of interacting material points (consistent with the reconstruction grid), which obeys a cohesive law directly obtained from basic constitutive relationships with analytical solutions. The interactions among the material points include both local pair-wise potential between two particles U_{pair} and a multi-body potential among non-local particles U_V, i.e., $U = U_{pair} + U_V$. Accordingly, the force field between two neighboring particles only depends on their relative displacements (i.e., pair-wise potential), but also includes a contribution from all the neighboring particles surrounding them (i.e., non-local multi-body potential). The unique advantage of the LPM formulation is that material fracture can be naturally simulated by breaking the bonds between material points based on critical bond length or force. The LPM has been successfully applied to study the mechanical performance of a variety of heterogeneous material systems [64–66]. Interested readers are referred to Refs. [62, 63] for details of this method.

B. Elastic behavior

We now apply the LPM to study the mechanical properties of the reconstructed hyperuniform materials. Specifically, we consider the inclusion phase serves as the reinforcement for the matrix, and both phases are isotropic. The Young's modulus and Poisson's ratio for the inclusion and matrix phase are respectively $E_I = 100$ GPa, $\mu_I = 0.33$ and $E_M = 10$ GPa, $\mu_M = 0.32$. We note that the exact values of the mechanical properties of individual phases do not affect the conclusions of our study, yet the contrast between the Young's moduli of the inclusion and matrix phases does affect the degree of contrast between the effective moduli of the hyperuniform and the corresponding non-hyperuniform materials. A uniaxial load is applied to the top and bottom boundary of the square representative volume element (RVE) reconstructed in Sec. IV, which leads to an overall axial elastic strain $\epsilon = 0.002$. The remaining two boundaries of the RVE are force free. In the subsequent LPM simulations, we will focus on the systems with $\phi = 0.3$ for which the inclusion phase forms a dispersion of compact clusters and particles, in contrast to the nearly percolating morphology of the inclusion phase for the systems with $\phi = 0.5$. Thus, we expect to observe more significant contrast between the mechanical behaviors of the hyperuniform and non-hyperuniform systems with $\phi = 0.3$.

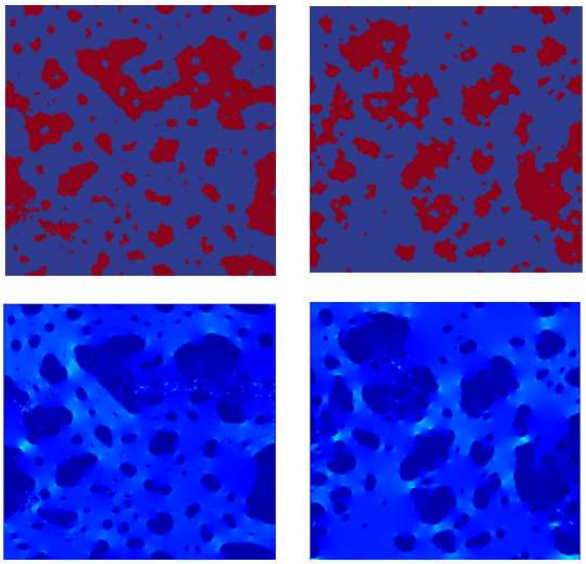

FIG. 6: Elastic strain energy density distribution $\Omega(\mathbf{x})$ in a hyperuniform material (left panels) associated with the exponential decay function (with $\gamma = 50$) and its non-hyperuniform counterpart (right panels).

Figure 6 shows an example of the elastic strain energy density distribution $\Omega(\mathbf{x})$ in a hyperuniform material associated with the exponential decay function (with $\gamma = 50$) and its non-hyperuniform counterpart. Figure 7 shows the associated statistics of the strain energy density distribution $f(\Omega)$ in both systems. It can be seen that the high strain energy densities usually occur in regions with a high degree of clustering of the inclusion phases in both systems. In addition, the quantitative

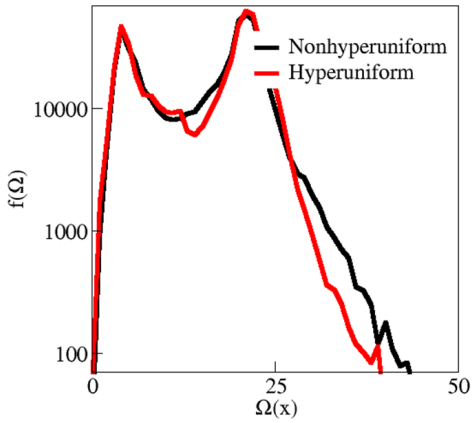

FIG. 7: Statistics of the strain energy density distribution $f(\Omega)$ in the hyperuniform system (red curve or light gray curve in print version) and non-hyperuniform system (black curve) as shown in Fig. 6.

statistics indicate that the non-hyperuniform system possesses a significantly larger population of high strain energy density values compared to its hyperuniform counterpart, which would be due to the distinct large-scale structural characteristics of the two systems.

Figure 8 shows the averaged local strain energy density $\bar{\Omega}$ defined as

$$\bar{\Omega} = \frac{1}{V}\int \Omega(\mathbf{x}) d\mathbf{x}, \tag{24}$$

where V is the volume of the system, for systems associated with both the hard sphere function $f^{HS}(r)$ and the exponential decay function $f^{ED}(r)$ for different cutoff distances γ. It can be seen that for both correlation functions, the non-hyperuniform systems generally possess a larger $\bar{\Omega}$ compared to the corresponding hyperuniform systems, which would be mainly due to the excessive number of high Ω states in the former. Figure 9 shows the normalized effective Young's modulus $\bar{E}/E_M$ of the reconstructed heterogeneous materials, i.e., $\bar{E} = \bar{\sigma}/\epsilon$, where $\bar{\sigma}$ is the average tensile stress in the system and ϵ is the applied tensile strain. Consistent with the trends in $\bar{\Omega}$, we see again that the non-hyperuniform systems generally possess a higher $\bar{E}$ compared to the corresponding hyperuniform systems. A possible reason for the observed smaller $\bar{\Omega}$ and $\bar{E}$ in hyperuniform systems considered here is the higher degree of uniformity in the distribution of clusters on large length scales. This would effectively lead to a lower degree of stress concentration in such systems and thus, an overall lower elastic energy and smaller modulus.

It is interesting to note that the contrast between $\bar{E}$ of the hyperuniform and non-hyperuniform systems associated with the exponential decay function f^{ED} is significantly stronger than that for systems associated with the hard sphere function f^{HS}. As discussed in Sec. IV, due to the nature of f^{HS} and the associated original equilibrium hard sphere system that is close to hyperuniformity,

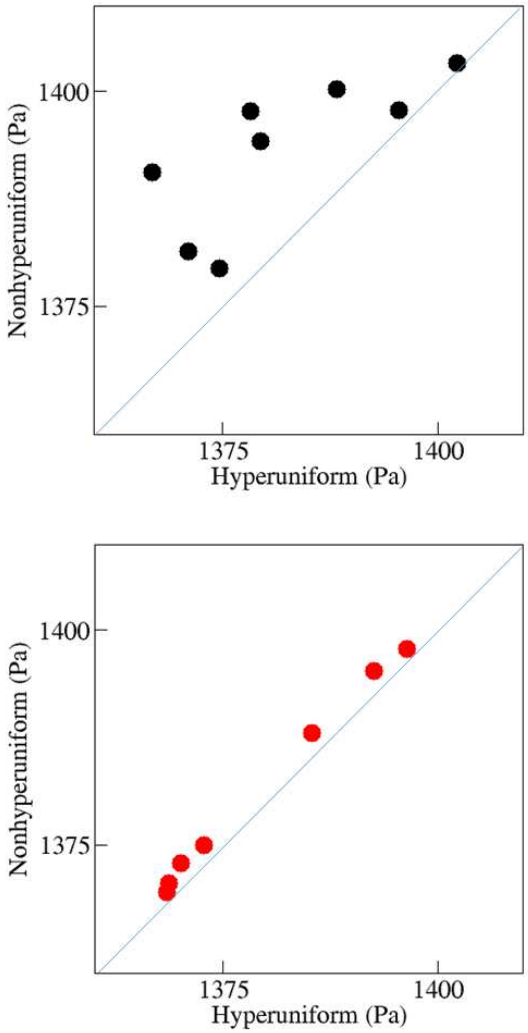

FIG. 8: Averaged elastic strain energy density $\bar{\Omega}$ in the reconstructed materials associated with the exponential decay function $f^{ED}(r)$ (upper panel) and the hard sphere function $f^{HS}(r)$ (lower panel) for different γ values.

the structural distinctions between the hyperuniform and non-hyperuniform systems associated with f^{HS} are much smaller on both small and large length scales. This has led to a weaker contrast between $\bar{\Omega}$ of the hyperuniform and non-hyperuniform systems and thus, a weaker contrast between $\bar{E}$.

C. Brittle fracture analysis

We now study the brittle fracture behavior of the reconstructed systems. As briefly discussed in Sec. V.A, in the LPM the continuum is modeled as a regular array of material points interacting with near neighbors and thus, fracture is naturally captured via breaking of bonds between the material points. The same Young's modulus and Poisson's ratio for the inclusion and matrix phases

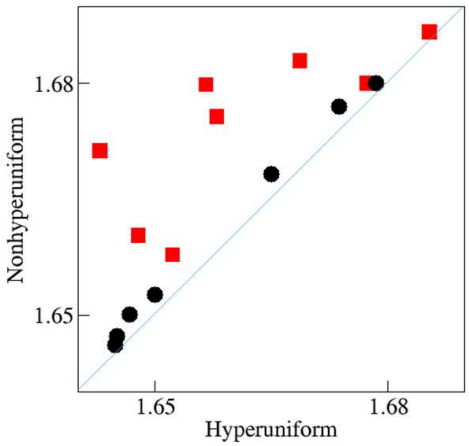

FIG. 9: Normalized effective Young's modulus $\bar{E}/E_M$ of the reconstructed heterogeneous materials associated with the exponential decay function $f^{ED}(r)$ (red square or light gray square in print version) and the hard sphere function $f^{HS}(r)$ (black circle) for different γ values.

as in Sec. V.B are also used here. In addition, the critical stress for bond breaking is set to be $\sigma_c = 950$ MPa. We note that similar to the elastic analysis, although the exact value of the fracture strength σ_f depends on the choice of σ_c, the conclusions drawn here are not affected by σ_c. A uniaxial load is applied to the square RVE of the reconstructed materials under the quasi-static loading condition, with a strain rate $d\epsilon/dt = 10^{-7}$ per loading step and a total of $N = 40,000$ loading steps are used. After each loading step, the stress and strain distributions in the RVE are computed and each bond is checked for possible breaking. If the stress in a bond is greater than the critical stress σ_c, this bond (i.e., the connection between two materials points) is removed from the system, which corresponds to the nucleation of a micro-void. This will lead to a significant change of the stresss/strain distributions in the next loading step. The reaction force F (and the uniaxial tensile stress) is computed at each loading step. The material is consider to fail when a abrupt drop is observed in F. The fracture strength is then computed from the maximum reaction force, i.e., $\sigma_f = F_{max}/A$, where A is the cross-sectional area of the RVE.

Figure 10 shows an example of our brittle fracture simulations of the reconstructed hyperuniform material and its non-hyperuniform counterpart associated with $f^{ED}(r)$ and $\gamma = 50$ pixels. The corresponding reaction forces as a function of tensile strain ϵ_T is shown in Fig. 11, which is overall an increasing function of ϵ_T. We note that the small oscillations in the $F-\epsilon_T$, which are due to the dynamic method for solving the LPM equations and will vanish in the limit of zero strain rate, do not affect the calculation of the fracture strength. It can be clearly seen in Fig. 11 that the hyperuniform material possesses a much higher maximal reaction force F_{max} and thus, a higher fracture strength σ_f than the corresponding non-

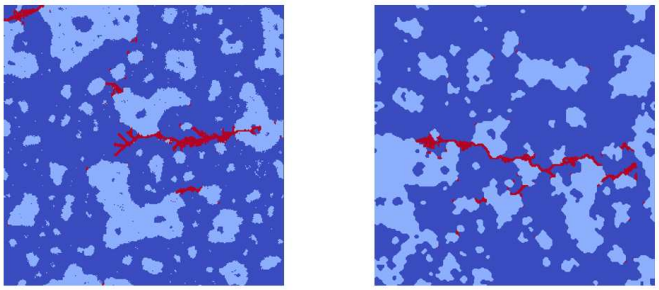

FIG. 10: Growing cracks in the reconstructed hyperuniform material (left) and its non-hyperuniform counterpart (right) associated with $f^{ED}(r)$ and $\gamma = 50$ pixels generated using LPM simulations.

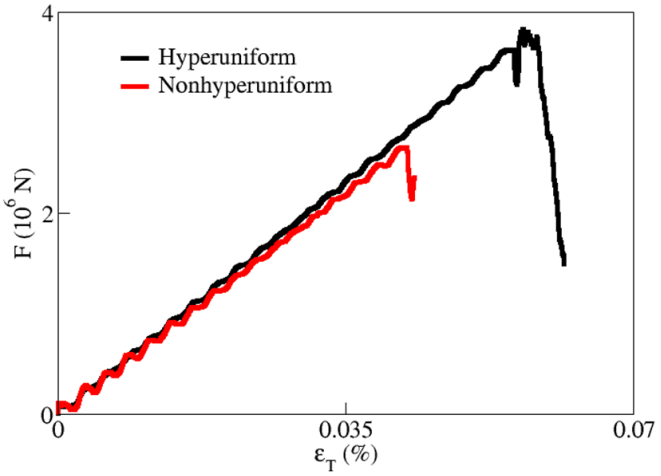

FIG. 11: Reaction forces as a function of tensile strain ϵ_T in the two materials (red curve or light gray curve in print version for non-hyperuniform system, black curve for hyperuniform system) shown in Fig. 10 under quasi-static uniaxial loading condition.

hyperuniform material.

The same analysis is applied to all systems with $\phi = 0.3$ reconstructed in Sec. IV, and the obtained fracture strengths of the hyperuniform materials vs. the corresponding non-hyperuniform materials are shown in Fig. 12. We can see that for the systems associated with the exponential decay function $f^{DE}(r)$, the hyperuniform systems generally possess a higher fracture strength σ_f than the corresponding non-hyperuniform systems. Specifically, σ_f of the hyperuniform materials can be larger than that for the corresponding non-hyperuniform materials by as large as 20%. However, for systems with the hard sphere function $f^{HS}(r)$, the hyperuniform systems possess similar and even slightly smaller σ_f compared to their corresponding non-hyperuniform counterparts. We note that this observation is also consistent with the trend observed in the effective Young's modulus, i.e., the contrast between the hyperuniform and non-

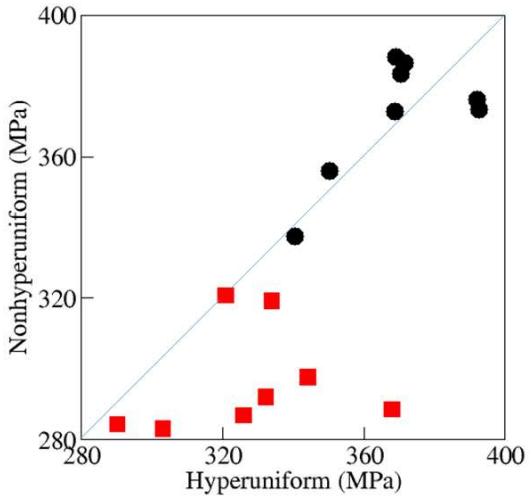

FIG. 12: Fracture strengths of the hyperuniform materials vs. the corresponding non-hyperuniform materials associated with the exponential decay function $f^{ED}(r)$ (red square or light gray square in print version) and the hard sphere function $f^{HS}(r)$ (black circle).

hyperuniform systems associated with the exponential decay function is generally larger than that for systems associated with the hard sphere function. This again is attributed to the smaller structural distinctions between the hyperuniform and non-hyperuniform systems associated with $f^{HS}(r)$ on both small and large length scales.

To understand why hyperuniform materials generally possess superior brittle fracture behavior, we further examine the mechanisms for the nucleation and growth of the cracks in the reconstructed systems. Specifically, due to the larger population of local high strain energy states in the non-hyperuniform materials, it is expected that a larger number of cracks are nucleated in such systems compared to their hyperuniform counterparts at the same loading level. This is evident from Fig. 10, which shows the distribution of cracks before the overall material failure occurs. It can be seen that the hyperuniform material contains a single major crack in the matrix phase, which indicates the failure is mainly due to the continuous growth of individual dominant cracks in the system. In contrast, the non-hyperuniform material contains a large number of smaller cracks, which start to connect to one another and form a percolating large crack across the entire system. Therefore, the major failure mechanism in the non-hyperuniform materials is the fast growth and percolation of many small cracks, which under the same loading condition leads to a lower fracture strength than that of the corresponding hyperuniform materials.

VI. CONCLUSIONS AND DISCUSSIONS

In this paper, we have employed a stochastic optimization procedure to systematically generate realizations of hyperuniform heterogeneous materials, whose short-range orders are partially controlled by two distinct two-point correlation functions, i.e., the exponential decay function f^{ED} and the hard sphere function f^{HS}. For purpose of comparison, corresponding non-hyperuniform materials possessing the same partial short-range order (i.e., possessing the same correlation function up to the cut-off distance γ) have also been reconstructed and analyzed. We found that the partial short-range correlations imposed by the oscillating hard sphere function f^{HS} are compatible with the constraint on large-scale local volume fraction fluctuations and thus, hyperuniformity is more easily achieved in the systems associated with f^{HS}. On the other hand, the positive exponential function f^{ED} is not compatible with the hyperuniform constraint and the reconstructed hyperuniform and non-hyperuniform materials associated with this function possess distinct structural characteristics on large length scales.

In addition, we have investigated the mechanical performance of the reconstructed hyperuniform materials and their non-hyperuniform counterparts including both elastic and failure behaviors using the LPM simulations. For the constructed systems with partial short-range order consistent with the two specific correlation functions considered here, we found that the hyperuniform materials generally possess a smaller Young's modulus than their non-hyperuniform counterparts. However, the hyperuniform materials are found to be more resistent to brittle fracture, with a significantly higher fracture strength compared to the corresponding non-hyperuniform materials. This superior mechanical behavior is attributed to the lower degree of stress concentration in the material resulting from the hyperuniform microstructure, which results in different failure mechanisms in different systems. We emphasize our conclusion that a hyperuniform material is softer than its non-hyperuniform counterpart is restricted to the specific systems studied here. Generally, it can be expected a carefully designed hyperuniform material can certainly be made much stiffer than its nonhyperuniform counterpart.

Designing heterogeneous materials with superior mechanical properties especially failure resistance is a topic of great interest. Our study here suggests a possible avenue to achieving this goal, i.e., by imposing hyperuniformity in the system. The realizations of the hyperuniform materials can be easily fabricated using 3D printing. It is also interesting to see whether existing materials with a high fracture resistance such as certain natural and synthesized composites [67–69] would possess a nearly hyperuniform microstructure.

Acknowledgments

This work is partially supported by NSF CMMI under grant No. 1651147 (Program Manager: Mary Toney). Y. J. thank Arizona State University for the generous start-

up funds. W. X. is supported by National Natural Science Foundation Project of China (Grant No. 11402076).

[1] S. Torquato and F. H. Stillinger, Local density fluctuations, hyperuniform systems, and order metrics, Phys. Rev. E **68**, 041113 (2003).

[2] C. E. Zachary and S. Torquato, Hyperuniformity in point patterns and two-phase heterogeneous media, J. Stat. Mech.: Theory Exp. (2009) P12015.

[3] A. Gabrielli, M. Joyce, and F. Sylos Labini,Glass-like universe: Real-space correlation properties of standard cosmological models, Phys. Rev. D **65**, 083523 (2002).

[4] A. Donev, F. H. Stillinger, and S. Torquato, Unexpected density fluctuations in disordered jammed hard-sphere packings, Phys. Rev. Lett. **95**, 090604 (2005).

[5] C. E. Zachary, Y. Jiao, and S. Torquato, Hyperuniform long-range correlations are a signature of disordered jammed hard-particle packings, Phys. Rev. Lett. **106**, 178001 (2011).

[6] Y. Jiao and S. Torquato, Maximally random jammed packings of Platonic solids: Hyperuniform long-range correlations and isostaticity, Phys. Rev. E **84**, 041309 (2011).

[7] D. Chen, Y. Jiao, and S. Torquato, Equilibrium phase behavior and maximally random jammed state of truncated tetrahedra, J. Phys. Chem. B **118**, 7981 (2014).

[8] C. E. Zachary and S. Torquato, Anomalous local coordination, density fluctuations, and void statistics in disordered hyperuniform many-particle ground states, Phys. Rev. E **83**, 051133

[9] S. Torquato, G. Zhang, and F. H. Stillinger, Ensemble theory for stealthy hyperuniform disordered ground states, Phys. Rev. X **5**, 021020 (2015).

[10] O. U. Uche, F. H. Stillinger, and S. Torquato, Constraints on collective density variables: Two dimensions, Phys. Rev. E **70**, 046122 (2004).

[11] R. D. Batten, F. H. Stillinger, and S. Torquato, Classical disordered ground states: Super-ideal gases, and stealth and equi-luminous materials, J. Appl. Phys. **104**, 033504 (2008);

[12] R. D. Batten, F. H. Stillinger, and S. Torquato, Novel low-temperature behavior in classical many-particle systems, Phys. Rev. Lett. **103**, 050602 (2009).

[13] J. L. Lebowitz, Charge fluctuations in Coulomb systems, Phys. Rev. A **27**, 1491 (1983).

[14] G. Zhang, F. Stillinger, and S. Torquato, Ground states of stealthy hyperuniform potentials. I. Entropically favored configurations, Phys. Rev. E **92**, 022119 (2015).

[15] G. Zhang, F. Stillinger, and S. Torquato, Ground states of stealthy hyperuniform potentials: II. Stacked-slider phases, Phys. Rev. E **92**, 022120 (2015).

[16] L. Berthier, P. Chaudhuri, C. Coulais, O. Dauchot, and P. Sollich, Suppressed compressibility at large scale in jammed packings of size-disperse spheres, Phys. Rev. Lett. **106**, 120601 (2011).

[17] R. Kurita and E. R. Weeks, Incompressibility of polydisperse random-close-packed colloidal particles, Phys. Rev. E **84**, 030401 (2011).

[18] G. L. Hunter and E. R. Weeks, The physics of the colloidal glass transition, Rep. Prog. Phys. **75**, 066501 (2012).

[19] R. Dreyfus, Y. Xu, T. Still, L. A. Hough, A. G. Yodh, and S. Torquato, Diagnosing hyperuniformity in two-dimensional, disordered, jammed packings of soft spheres, Phys. Rev. E **91**, 012302 (2015).

[20] D. Hexner and D. Levine, Hyperuniformity of critical absorbing states, Phys. Rev. Lett. **114**, 110602 (2015).

[21] R. L. Jack, I. R. Thompson, and P. Sollich, Hyperuniformity and phase separation in biased ensembles of trajectories for diffusive systems, Phys. Rev. Lett. **114**, 060601 (2015).

[22] J. H.Weijs, R. Jeanneret, R. Dreyfus, and D. Bartolo, Emergent hyperuniformity in periodically driven emulsions, Phys. Rev. Lett. **115**, 108301 (2015).

[23] E. Tjhung and L. Berthier, Hyperuniform density fluctuations and diverging dynamic correlations in periodically driven colloidal suspensions, Phys. Rev. Lett. **114**, 148301 (2015).

[24] S. Torquato,A. Scardicchio, and C. E. Zachary, Point processes in arbitrary dimension from fermionic gases, random matrix theory, and number theory, J. Stat. Mech.: Theory Exp. (2008) P11019.

[25] R. P. Feynman and M. Cohen, Energy spectrum of the excitations in liquid helium, Phys. Rev. **102**, 1189 (1956).

[26] Y. Jiao, T. Lau, H. Hatzikirou, M. Meyer-Hermann, J. C. Corbo, and S. Torquato,Avian photoreceptor patterns represent a disordered hyperuniform solution to a multiscale packing problem, Phys. Rev. E **89**, 022721 (2014).

[27] A. Mayer, V. Balasubramanian, T. Mora, and A. M. Walcza, How a well-adapted immune system is organized, Proc. Natl. Acad. Sci. USA **112**, 5950 (2015).

[28] M. Hejna, P. J. Steinhardt, and S. Torquato, Nearly hyperuniform network models of amorphous silicon, Phys. Rev. B **87**, 245204 (2013).

[29] R. Xie, G. G. Long, S. J. Weigand, S. C. Moss, T. Carvalho, S. Roorda, M. Hejna, S. Torquato, and P. J. Steinhardt, Hyperuniformity in amorphous silicon based on the measurement of the infinite-wavelength limit of the structure factor, Proc. Natl. Acad. Sci. USA **110**, 13250 (2013).

[30] M. Florescu, S. Torquato, and P. J. Steinhardt, Designer disordered materials with large complete photonic band gaps, Proc. Natl. Acad. Sci. USA **106**, 20658 (2009).

[31] W. Man, M. Florescu, K. Matsuyama, P. Yadak, G. Nahal, S. Hashemizad, E. Williamson, P. Steinhardt, S. Torquato, and P. Chaikin, Photonic band gap in isotropic hyperuniform disordered solids with low dielectric contrast, Opt. Express **21**, 19972 (2013).

[32] W. Man, M. Florescu, E. P. Williamson, Y. He, S. R. Hashemizad, B. Y. C. Leung, D. R. Liner, S. Torquato, P. M. Chaikin, and P. J. Steinhardt, Isotropic band gaps and freeform waveguides observed in hyperuniform disordered photonic solids, Proc. Natl. Acad. Sci. USA **110**, 15886 (2013).

[33] G. Zhang, F. H. Stillinger, and S. Torquato, Transport, Geometrical, and topological properties of stealthy disordered hyperuniform two-phase systems, J. Chem. Phys. **145**, 244109 (2016).

[34] S. Torquato, Disordered hyperuniform heterogeneous

materials, J. Phys.: Condensed Matt., **28**, 414012 (2016).
[35] S. Torquato, Hyperuniformity and its generalizations, Phys. Rev. E **94**, 022122 (2016).
[36] J. Haberko, N. Muller, and F. Scheffold, Direct laser writing of three dimensional network structures as templates for disordered photonicmaterials, Phys. Rev. A **88**, 043822 (2013).
[37] G. Zito, G. Rusciano, G. Pesce, A. Malafronte, R. Di Girolamo, G. Ausanio, A. Vecchione, and A. Sasso, Nanoscale engineering of two-dimensional disordered hyperuniform blockcopolymer assemblies, Phys. Rev. E **92**, 050601 (2015).
[38] C. L. Y. Yeong and S. Torquato, Reconstructing random media, Phys. Rev. E **57**, 495 (1998).
[39] S. Torquato, Microstructure characterization and bulk properties of disordered two-phase media, J. Stat. Phys. **45**, 843 (1986).
[40] S. Torquato, *Random Heterogeneous Materials: Microstructure and Macroscopic Properties*, New York: Springer (2002).
[41] Y. Jiao, F. H. Stillinger, and S. Torquato, Modeling heterogeneous materials via two-Point correlation functions: Basic principles, Phys. Rev. E. **76**, 031110 (2007).
[42] Y. Jiao, F. H. Stillinger, and S. Torquato, Modeling heterogeneous materials via two-point correlation functions: II. Algorithmic details and applications, Phys. Rev. E **77**, 031135 (2008).
[43] Y. Jiao, F. H. Stillinger, and S. Torquato, A superior descriptor of random textures and its predictive capacity, Proc. Natl. Acad. Sci. **106**, 17634 (2009).
[44] C. Gommes, Three-dimensional reconstruction of liquid phases in disordered mesopores using in situ small-angle scattering, J. Appl. Crystal. **46**, 493 (2013).
[45] A. P. Roberts, Statistical reconstruction of three-dimensional porous media from two- dimensional images, Phys. Rev. E **56**, 3203 (1997).
[46] D. T. Fullwood, S. R. Kalidindi, S. R. Niezgoda, A. Fast, and N. Hampson, Gradient-based microstructure reconstructions from distributions using fast Fourier transforms, Mater. Sci. Eng. A **494**, 68 (2008)
[47] D. T. Fullwood, S. R. Niezgoda, and S. R. Kalidindi, Microstructure reconstructions from 2-point statistics using phase-recovery algorithms, Acta Mater. **56**, 942 (2008).
[48] A. Hajizadeh , A. Safekordi, and F. A. Farhadpour, A multiple-point statistics algorithm for 3D pore space reconstruction from 2D images, Adv. Water. Res. **34**, 1256 (2011).
[49] P. Tahmasebi and M. Sahimi, Cross-correlation function for accurate reconstruction of heterogeneous media, Phys. Rev. Lett. **110**, 078002 (2013).
[50] M. G. Rozman and U. Utz, Uniqueness of reconstruction of multiphase morphologies from two-point correlation functions, Phys. Rev. Lett. **89**, 135501 (2002).
[51] T. Tang, Q. Teng, X. He and D. Luo, A pixel selection rule based on the number of differentphase neighbours for the simulated annealing reconstruction of sandstone microstructure, J. Microscopy **234**, 262 (2009).
[52] L. M. Pant, S. K. Mitra, and M. Secanell, Stochastic reconstruction using multiple correlation functions with different-phase-neighbor-based pixel selection, Phys. Rev. E **90**, 023306 (2014).
[53] Y. Jiao, E. Pallia, and N. Chawla, Modeling and predicting microstructure evolution in lead/tin alloy via correlation functions and stochastic material reconstruction, Acta Mater. **61**, 3370 (2013).
[54] S. Singh, J. J. Williams, Y. Jiao, and N. Chawla, Modeling anisotropic multiphase heterogeneous materials via direction correlation functions: Simulations and experimental verification, Metall. Mater. Trans. A **43**, 4470 (2012).
[55] K. M. Gerke, M. V. Karsanina, R. V. Vasilyev, and D. Mallants, Improving pattern reconstruction using directional correlation functions, EPL **106**, 66002 (2014).
[56] Y. Jiao and N. Chawla, Modeling and characterizing anisotropic inclusion orientation in heterogeneous material via directional cluster functions and stochastic microstructure, J. Appl. Phys. **115**, 093511 (2014).
[57] H. Li, N. Chawla, and Y. Jiao Reconstruction of heterogeneous materials via stochastic optimization of limited-angle X-ray tomographic projections, Scripta Mater. **86**, 48 (2014).
[58] S. Chen, H. Li, and Y. Jiao Dynamic reconstruction of heterogeneous materials and microstructure evolution, Phys. Rev. E **92**, 023301 (2015).
[59] H. Li, C. S. Kaira, J. Mertens, N. Chawla, and Y. Jiao Accurate stochastic reconstruction of heterogeneous microstructures by limited X-ray tomographic projections, J. Microscopy **264**, 339 (2016).
[60] S. Chen, A. Kirubanandham, N. Chawla and Y. Jiao Stochastic multi-scale reconstruction of 3D microstructure consisting of polycrystalline grains and second-phase particles from 2D micrographs, Metall. Mater. Trans. A **47**, 1440 (2016).
[61] S. Kirkpatrick, C. D. Gelatt, and M. P. Vecchi, Optimization by simulated annealing, Science **220**, 671 (1983).
[62] H. Chen, E. Lin, Y. Jiao, and Y. Liu, A generalized 2D non-Local lattice spring model for fracture simulation, Comput. Mech. **54**, 1541 (2014).
[63] H. Chen, Y. Jiao and Y. Liu, A nonlocal lattice particle model for fracture simulation of anisotropic materials, Composites Part B **90**, 141 (2016).
[64] H. Chen, Y. Jiao, and Y. Liu, Investigating the microstructural effect on elastic and fracture behavior of polycrystals using a nonlocal lattice-particle model, Mater.Sci. Eng. A **631**, 173 (2015).
[65] H. Chen, Y. Xu, Y. Jiao and Y. Liu, A novel discrete computational tool for microstructure-sensitive mechanical analysis of composite materials, Mater.Sci. Eng. A **659**, 234 (2016).
[66] H. Chen, L. Meng, S. Chen, Y. Jiao and Y. Liu, Numerical investigation of microstructure effect on mechanical properties of bi-continuous and particulate reinforced composite materials, Comput. Mater. Sci. **122**, 288 (2016).
[67] W.X. Xu, F. Wu, Y. Jiao, M. Liu, A general micromechanical framework of effective moduli for the design of nonspherical nano- and micro-particle reinforced composites with interface properties. Materials & Design **127**, 162 (2017).
[68] W.X. Xu, H.F. Ma, S.Y. Ji, H.S. Chen, Analytical effective elastic properties of particulate composites with soft interfaces around anisotropic particles, Compos. Sci. Technol. **129**, 10 (2016).
[69] W.X. Xu, B. Xu, F. Guo, Elastic properties of particle-reinforced composites containing nonspherical particles of high packing density and interphase: DEM-FEM simulation and micromechanical theory. Computer Methods in Applied Mechanics and Engineering **326**, 122 (2017).